

Single Pair of Charge-two Weyl Fermions in Chiral Boron Allotropes

Hui-Jing Zheng¹, Yan Gao^{1*}, Yanfeng Ge¹, Yong Liu¹, and Zhong-Yi Lu^{2,3}

¹State Key Laboratory of Metastable Materials Science and Technology & Hebei Key Laboratory of Microstructural Material Physics, School of Science, Yanshan University, Qinhuangdao 066004, China

²School of Physics and Beijing Key Laboratory of Opto-electronic Functional Materials & Micro-nano Devices, Renmin University of China, Beijing 100872, China

³Key Laboratory of Quantum State Construction and Manipulation (Ministry of Education), Renmin University of China, Beijing 100872, China

The realization of a minimal Weyl semimetal (WSM) hosting a single pair of Weyl points (WPs) has thus far been restricted to magnetic systems, since time-reversal symmetry generally enforces a minimum of four WPs in nonmagnetic materials. Here, combining first-principles calculations with symmetry analysis, we identify two stable boron allotropes, chiral HDSBC-B₂₀ and cage-like CR-B₁₂, as the first nonmagnetic electronic materials realizing a single pair of WPs in the spinless regime. We show that the interplay between time-reversal symmetry and crystallographic rotation symmetry (C_4 or C_3) stabilizes exactly one pair of charge-2 WPs pinned at time-reversal-invariant momenta, thereby circumventing the conventional node-quartet constraint. These double-WPs exhibit linear dispersion along the rotation axis and quadratic dispersion in the perpendicular plane. In HDSBC-B₂₀, the sign of the topological charge is directly correlated with structural chirality. Both materials host exceptionally long double Fermi arcs spanning the surface Brillouin zone, providing experimentally accessible signatures. Our findings establish nonmagnetic material platforms for minimal double-Weyl fermions and broaden the landscape of unconventional WSMs.

*Corresponding authors: yangao9419@ysu.edu.cn

Introduction

The discovery of Weyl semimetals (WSMs) has opened a new frontier in condensed matter physics¹⁻⁴, providing a solid-state realization of Weyl fermions⁵⁻⁷ and giving rise to a host of topological phenomena, including the chiral anomaly^{8, 9}, topological Fermi-arc surface states¹⁻³, quantum anomalous Hall effect¹⁰, and negative magnetoresistance effect^{11, 12}. These phenomena originate from bulk Weyl points (WPs)⁵, which act as monopoles of Berry curvature in momentum space and are characterized by quantized topological charges, or Chern numbers C . Conventional WPs with $|C| = 1$ exhibit linear band dispersion along all momentum directions, whereas unconventional multi-Weyl points¹³ with higher chiral charges ($|C| = 2, 3, 4$) display anisotropic dispersions in which two distinct orders of momentum dependence, among linear, quadratic, and cubic, are combined¹⁴. Such higher-charge WPs are necessarily stabilized by crystalline rotational symmetries¹³⁻¹⁶ and are expected to host enhanced topological responses, including longer Fermi arc surface states¹⁷, quantum criticality and phase transition¹⁸, larger quantized circular photogalvanic effect¹⁹, and possible deviations from Fermi-liquid behavior²⁰. A central objective in Weyl physics is the realization of minimal WSMs hosting the fewest possible WPs, ideally a single pair. Such minimal configurations avoid the complications introduced by multiple WPs and provide the conceptually cleanest setting for establishing bulk-boundary correspondence.

However, in nonmagnetic systems this goal is strongly constrained by the Nielsen–Ninomiya no-go theorem^{21, 22}. Time-reversal symmetry (\mathcal{T}) enforces the appearance of WPs with identical chirality at \mathbf{k} and $-\mathbf{k}$, thereby requiring at least four WPs (two pairs) to satisfy overall topological charge neutrality²³⁻²⁸. Consequently, circumventing this “four-node” barrier to realize a minimal WSM hosting only a single Weyl-point pair has emerged as a key frontier in the field. Although theoretical strategies have been proposed to circumvent this limitation by pinning WPs at time-reversal-invariant momenta (TRIMs), a mechanism permitting a single-pair $|C| = 2/4$ WPs in the

spinless systems²⁹, experimental and theoretical material realizations have thus far been largely restricted to bosonic systems^{30, 31}. Magnetic systems can bypass this constraint by breaking \mathcal{T} to host a single Weyl pair, as exemplified by β -V₂OPO₄³², K₂Mn₃(AsO₄)₃³³, EuAgP³⁴, EuCd₂As₂³⁵ and MnSn₂Sb₂Te₆-B³⁶. While these works have significantly advanced the understanding of minimal Weyl configurations, the resulting WPs are inextricably tied to magnetic ordering, which is often realized only under specific conditions such as low temperatures or finely tuned magnetic structures. In the nonmagnetic electronic realm, however, realizing a pristine minimal Weyl state remains an elusive goal, frequently obscured by strong spin-orbit coupling (SOC) and the entanglement of trivial bands near the Fermi level^{37, 38}.

In this work, combining first-principles calculations with symmetry analysis, we overcome this challenge by identifying two boron allotropes, chiral HDSBC-B₂₀ and cage-structured CR-B₁₂, that realize the long-sought single pair of double-Weyl fermions in a nonmagnetic electronic environment. Both structures are demonstrated to be dynamically, thermally, and mechanically stable, with CR-B₁₂ notably exhibiting a formation energy lower than many topological boron phases and even experimentally synthesized α -Ga boron. Crucially, the electronic structure near the Fermi level is pristine: the valence and conduction bands intersect exclusively at two distinct TRIMs, forming a single pair of $|C| = 2$ WPs protected by C_4/C_3 rotation and \mathcal{T} , free from any coexisting trivial Fermi pockets. In chiral HDSBC-B₂₀, the sign of the Weyl-point topological charge is strictly dictated by the structural handedness, establishing a direct link between real-space chirality and momentum-space topology. The large separation of the WPs, combined with their double charge, generates “maximal” double Fermi arcs that traverse the surface Brillouin zone (BZ), offering unambiguous experimental fingerprints. Our findings establish an ideal platform for investigating minimal $|C| = 2$ Weyl fermions and open a new paradigm for realizing unconventional Weyl physics in light-element, nonmagnetic systems.

Results

The structural versatility of boron allows for the formation of complex three-dimensional (3D) networks. Here, we identify two distinct metastable boron allotropes. The first, HDSBC-B₂₀, crystallizes in the chiral tetragonal space groups $P4_3$ (No. 78) for left-handed *l*-HDSBC-B₂₀ [Fig. 1(a)] and $P4_1$ (No. 76) for right-handed *r*-HDSBC-B₂₀ [Fig. 1(b)]. These enantiomers, related by spatial inversion, are characterized by homochiral boron chains of distinct widths: single-atom-width spiraling boron chains (SBC) [Fig. 1(c)] and double-atom-width helical chains (HD) [Fig. 1(d)] are interconnected via bridging atoms (green) to form a stable 3D network. Each primitive unit cell contains 20 boron atoms [Fig. 1(e)], hence the designation HDSBC-B₂₀ (Helical Double & Single Boron Chain). The second phase, CR-B₁₂, adopts the rhombohedral space group $R32$ (No. 155). Its primitive cell comprises a new type of B₁₂ icosahedral cages [Fig. 1(j)] forming a covalent cage-based network [Figs. 1(g)-1(h)], distinct from the conventional α -B₁₂ motif [Fig. 1(k)].

The optimized structural parameters are summarized in Table SI [see Supplemental Material (SM)]. Remarkably, CR-B₁₂ exhibits a formation energy of -6.52 eV/atom, which, while slightly higher than the near-ground-state α -B₁₂³⁹, is energetically lower than that of many proposed topological boron phases and even lower (by 0.11 eV/atom) than the experimentally synthesized α -Ga phase⁴⁰. Comprehensive stability analysis further confirms their viability: (i) Phonon dispersions show no imaginary frequencies across the BZ for CR-B₁₂ [Fig. 2(c)], and only exhibit negligible soft modes near Γ for HDSBC-B₂₀ (likely of numerical origin), collectively confirming the dynamical stability of both phases. (ii) *Ab initio* molecular dynamics simulations confirm the room-temperature thermodynamic stability of HDSBC-B₂₀, with no structural bond breaking observed at 300 K [Fig. 2(b)], while CR-B₁₂ remains structurally stable up to 900 K [Fig. 2(d)]. (iii) Mechanical stability is rigorously verified, as the calculated elastic stiffness constants C_{ij} fully satisfy the Born stability criteria⁴¹ for both tetragonal and trigonal symmetries [see Table SII in the SM].

We first examine the electronic structure of the chiral boron allotrope HDSBC-B₂₀. Because boron is a light element with intrinsically weak SOC, SOC effects are negligible, and the system can be accurately described within a spinless framework ($\mathcal{T}^2 = 1$). The band structure and projected density of states (PDOS) for *l*-HDSBC-B₂₀ are presented in Figs. 3(a) and 3(b), respectively. The PDOS exhibits a pronounced minimum near the Fermi level E_F , characteristic of semimetallic behavior. Inspection of the bulk bands reveals that the valence (band 30) and conduction (band 31) states touch exclusively at two isolated TRIMs in the BZ: W_1 at Γ ($E - E_F = 0.155$ eV) and W_2 at M ($E - E_F = -0.052$ eV). A comprehensive scan of the BZ confirms that a finite gap persists everywhere else between these two bands, strictly satisfying the minimal node count mandated by the Nielsen-Ninomiya theorem for a time-reversal invariant system.

Symmetry analysis of the Bloch states confirms the topological nature of these crossings. The irreducible representations at Γ and M correspond to the doubly degenerate $\Gamma_3\Gamma_4$ and M_3M_4 states of space group $P4_3$, respectively [Fig. 3(a)], identifying each node as a protected degeneracy. The band dispersions in the vicinity of W_1 and W_2 , plotted in the k_x-k_y plane [Figs. 3(c) and 3(d)], clearly exhibit quadratic dispersion in the transverse plane, while Fig. 3(a) reveals linear dispersion along the k_z (Γ -Z and M -A) direction. Such a linear-quadratic dispersion is the hallmark of double-Weyl fermions with topological charge $|C| = 2$.

To elucidate the symmetry protection mechanism, we construct a low-energy $\mathbf{k} \cdot \mathbf{p}$ effective model. At Γ point (W_1), the little group is C_4 within space groups $P4_3$ (No. 78), generated by fourfold rotation C_4 and time-reversal symmetry \mathcal{T} . In the basis of the $\Gamma_3\Gamma_4$ doublet, the matrix representations of symmetry operators are represented as $D(C_{4,001}^+) = i\sigma_z$ and $D(\mathcal{T}) = \sigma_x K$, where σ_i ($i = x, y, z$) are Pauli matrixes and K is the complex-conjugate operator. These generators impose the following constraints on the Hamiltonian:

$$D(g)H(\mathbf{k})D^{-1}(g) = H(g\mathbf{k}), \quad (1)$$

where g represents the generating elements of $C_{4,001}^+$ and \mathcal{T} . Hence, the two band $\mathbf{k} \cdot \mathbf{p}$ effective Hamiltonian expanded up to k^2 order is derived as

$$H_{W_1}(\mathbf{k}) = \varepsilon(\mathbf{k}) + [(\alpha k_+^2 + \beta k_-^2)\sigma_+ + \text{H.c.}] + mk_z\sigma_z, \quad (2)$$

where $\varepsilon(\mathbf{k}) = \epsilon_0 + \epsilon_1(k_x^2 + k_y^2) + \epsilon_2k_z^2$. ϵ_i ($i = 0,1,2$) and m are real parameters, while α and β are complex parameters, all determined by fitting to the DFT band structure of HDSBC-B₂₀. This model explicitly confirms that W_1 at Γ is a double-Weyl point with linear dispersion along k_z and quadratic dispersion in the k_x - k_y plane. An analogous symmetry analysis at the M point (W_2) yields an identical effective Hamiltonian, establishing the double-Weyl nature of W_2 as well. The optimized model parameters reproduce the DFT bands with excellent agreement [see Figs. S1(a) and S1(b) in the SM], validating the physical reliability of the effective model.

The topological charges of W_1 and W_2 are unambiguously determined by integrating the Berry curvature over a closed surface enclosing each node. We find $C = -2$ for W_1 and $C = +2$ for W_2 [Fig. 3(e)], satisfying the net topological charge neutrality. The Berry curvature distribution in the $k_z = 0$ plane [Fig. 3(f)] further visualizes W_2 as a Berry-curvature source and W_1 as a sink, in full consistency with their respective chiral charges.

Upon projecting the bulk WPs onto the (001) surface [Fig. 1(f)], we observe prominent Fermi-arc surface states crossing the Fermi level [Fig. 3(g)]. These arcs directly connect the projected WPs with opposite topological charges, providing a clear manifestation of the bulk-boundary correspondence. At the energy slice $E = -52$ meV, corresponding to the energy of W_2 , Fig. 3(h) reveals that the surface states consist of extended double Fermi arcs across the surface BZ, a direct consequence of the minimal single-pair double-WPs configuration. Calculations for the (100) surface [Fig. S2 in the SM] yield similarly long and extended double Fermi arcs. Together, both surfaces exhibit robust and distinctive signatures of a single pair of double-WPs, providing distinctive signals for future experimental detection.

For the right-handed counterpart r -HDSBC-B₂₀ [Figs. 3(i-p)], the overall electronic structure remains qualitatively identical to that of the left-handed l -HDSBC-B₂₀ [Figs. 3(i-l)]. Importantly, however, the chiralities of the WPs are reversed [Figs. 3(m-n)], in direct correspondence with the inversion of the crystal handedness. This one-to-one mapping between structural chirality and Weyl-point chirality provides a clear physical mechanism for controlling topological charge through crystal geometry, suggesting potential applications in chirality-dependent transport and optical responses. Consistent with this picture, r -HDSBC-B₂₀ also exhibits extended double Fermi arcs on both the (001) and (100) surfaces [Figs. 3(o-p) and Fig. S3 in the SM].

We next turn to the electronic structure and topological properties of CR-B₁₂, which exhibits a closely related but symmetry-distinct realization of single-pair double-Weyl fermions. Figures 4(a) and 4(b) show the band structure and PDOS, respectively. A pronounced minimum in the PDOS near the intrinsic Fermi level again indicates a semimetallic character. The valence-band maximum and conduction-band minimum (18th and 19th bands) intersect only at two points in the entire BZ: W_1 at Γ and W_2 at the T point. Irreducible-representation analysis reveals that W_1 and W_2 transform as the two-dimensional (2D) representations Γ_3 and T_3 , respectively, implying that both are doubly degenerate WPs. Energetically, W_1 is located 0.902 eV above E_F , while W_2 lies 0.133 eV below E_F [see Table SIII in the SM]. The PDOS indicates that the low-energy states near both WPs are dominated by boron p_z orbitals. As shown in Figs. 4(c) and 4(d), both W_1 and W_2 display quadratic dispersion in the k_x - k_y plane and linear dispersion along the threefold rotation axis (Γ -T direction), a characteristic signature of $|C| = 2$ WPs.

The effective Hamiltonian at Γ for space group $R32$ (D_3 point group) is constrained by $C_{3,001}^+$, $C_{2,100}$, and time-reversal symmetry \mathcal{T} . Under the Γ_3 basis, the corresponding matrix representations are

$$D(C_{3,001}^+) = \begin{bmatrix} e^{\frac{i2\pi}{3}} & 0 \\ 0 & e^{-\frac{i2\pi}{3}} \end{bmatrix}, \quad D(C_{2,100}) = \begin{bmatrix} 0 & e^{-\frac{i2\pi}{3}} \\ e^{\frac{i2\pi}{3}} & 0 \end{bmatrix}, \quad D(\mathcal{T}) = \sigma_x K. \quad (3)$$

These generators impose symmetry constraints on the Hamiltonian through Eq. (1). Expanding to leading order yields

$$H_{W_1}(\mathbf{k}) = \varepsilon(\mathbf{k}) + [(\alpha k_+^2 + \beta k_- k_z)\sigma_+ + \text{H. c.}] + mk_z\sigma_z, \quad (4)$$

where $\varepsilon(\mathbf{k}) = \varepsilon_0 + \varepsilon_1(k_x^2 + k_y^2) + \varepsilon_2k_z^2$. Fitting to the DFT bands confirms that W_1 at Γ is a double-Weyl point with quadratic in-plane and linear out-of-plane dispersion [Fig. S1(c)]. An analogous construction at the T point yields the same Hamiltonian form, establishing the double-Weyl nature of W_2 [Fig. S1(d)].

The chiral charges are determined by Berry-curvature integration, giving $C = +2$ for W_1 and $C = -2$ for W_2 [Fig. 4(e)]. The corresponding Berry-curvature distribution [Fig. 4(f)] identifies W_1 as a source and W_2 as a sink. Surface-state calculations reveal clear double Fermi arcs on the (001) surface at $E - E_F = 80$ meV [Figs. 4(g) and 4(h)], connecting the projections of W_1 and W_2 . Similar features are found on the (110) surface [Fig. S4 in the SM], demonstrating that these features are not surface-specific but instead represent a robust consequence of the bulk topology.

Discussion

A crucial aspect of the present study concerns the role and limitation of SOC. From a symmetry standpoint, it has been rigorously shown that a minimal Weyl configuration consisting of a single pair of charge-2 Weyl points in a nonmagnetic system is strictly allowed only in the spinless regime ($\mathcal{T}^2 = +1$), whereas the inclusion of SOC generally renders such a configuration symmetry-forbidden due to Kramers degeneracy and double-valued representations²⁹. In this sense, the spinless description adopted here is not merely a computational approximation but a fundamental requirement imposed by symmetry. This constraint also explains why previous searches for minimal WSMs in nonmagnetic electronic materials, largely focused on heavy-element systems with strong SOC, have so far been unsuccessful. Motivated by this consideration, our work targets light-element boron allotropes, whose intrinsically weak SOC enables the realization of this long-sought Weyl phase in an electronic setting. Explicit SOC

calculations show that SOC opens only extremely small gaps near the WPs of HDSBC-B₂₀ and CR-B₁₂, ranging from 0.08 meV to 1.19 meV (corresponding to energy scales of approximately 0.93–13.81 K) [see Fig. S5], which are negligible under typical experimental conditions. Therefore, the predicted single-pair double-Weyl fermions and their associated surface states remain physically relevant over a broad temperature range. These results establish light-element nonmagnetic systems with negligible SOC as an essential materials platform for realizing the simplest possible electronic WSM.

A symmetry-based mechanism for realizing a single pair of charge-2 Weyl points in spinless systems was previously proposed by Wang *et al.*²⁹. Our work advances this idea by demonstrating its realization in realistic nonmagnetic electronic materials and by revealing their concrete electronic and surface-state signatures. The identification of single-pair double-Weyl fermions in *l/r*-HDSBC-B₂₀ and CR-B₁₂ represents a substantial advance, establishing them as the first nonmagnetic electronic materials hosting this minimal $|C| = 2$ Weyl configuration. Previously reported $|C| = 2$ systems, such as (TaSe₄)₂I⁴², CaGe₂⁴³, and SrSi₂⁴⁴, contain multiple Weyl-point pairs, complicating the low-energy physics through inter-node coupling. While single-pair WPs have been realized in bosonic platforms such as chiral photonic and phononic crystals^{30, 31}, these systems inherently lack fermionic (electronic) degrees of freedom. Consequently, they cannot host electronic charge transport, enable electronic device functionalities, or couple directly to electromagnetic fields in the manner of WSMs. Magnetic WSMs, such as β -V₂OPO₄³², K₂Mn₃(AsO₄)₃³³, EuAgP³⁴, EuCd₂As₂³⁵ and MnSn₂Sb₂Te₆-B³⁶, achieve single-pair WPs configurations only under specific magnetic ordering conditions, typically at low temperatures.

In contrast, *l/r*-HDSBC-B₂₀ and CR-B₁₂ combine several decisive advantages: they are nonmagnetic and thus operable at room temperature; they are electronic systems supporting charge transport, optical responses, and field-effect tunability; their light-element composition leads to negligible SOC, enabling the realization of a single-pair WPs in a spinless setting; their low-energy electronic structures are exceptionally clean, involving only two bands near E_F ; the large momentum-space separation

between the WPs produces extraordinarily long double Fermi arcs readily accessible to ARPES and STM; in HDSBC- B₂₀, the Weyl-point chirality is intrinsically tied to the crystal handedness, opening avenues for chirality-dependent optoelectronic effects; and CR-B₁₂ exhibits formation energies comparable to experimentally synthesized boron allotropes, suggesting realistic synthetic feasibility.

In summary, we have theoretically identified two boron allotropes, HDSBC-B₂₀ and CR-B₁₂, as the first nonmagnetic electronic materials hosting a minimal single pair of double-Weyl fermions. Both systems host exactly one pair of WPs carrying topological charge $|C| = 2$ Weyl configurations protected by C_3/C_4 rotational and time-reversal symmetries and give rise to exceptionally long double Fermi arcs extending across the surface BZ. Our work not only enriches the physics of boron materials but also shifts the focus from magnetic or bosonic systems to nonmagnetic light-element electronic platforms in the search for the minimal Weyl semimetal.

Methods

Computational methods: The electronic structures of HDSBC-B₂₀ and CR-B₁₂ were investigated by using the projector augmented wave (PAW) method⁴⁵ as implemented in the VASP package⁴⁶ in the framework of density functional theory (DFT). The exchange-correlation potential was treated using the generalized gradient approximation (GGA) of Perdew-Burke-Ernzerhof (PBE) type⁴⁷. The plane-wave kinetic energy cutoff was set to 550 eV. Brillouin zone (BZ) integration utilized Γ -centered k -point meshes⁴⁸ of $4 \times 4 \times 6$ for HDSBC-B₂₀ and $8 \times 8 \times 8$ for CR-B₁₂. Convergence criteria for energy and forces were set to 10^{-6} eV and 10^{-3} eV/Å, respectively. Phonon dispersions were computed using the finite displacement method implemented in the PHONOPY package⁴⁹ on $3 \times 3 \times 3$ (HDSBC-B₂₀) and $2 \times 2 \times 2$ (CR-B₁₂) supercells, respectively. Thermal stability was verified via *ab-initio* molecular dynamics (AIMD) simulations in a canonical ensemble using a Nose-Hoover thermostat⁵⁰. Elastic stiffness constants C_{ij} derived using the energy-strain method⁵¹. Topological properties were analyzed using WannierTools codes⁵² based on

effective tight-binding models derived from maximally localized Wannier functions via Wannier90⁵³.

Data availability

The data supporting the findings are displayed in the main text and the Supplementary Information. All raw data are available from the corresponding authors upon request.

References:

1. Xu, S.-Y. et al. Discovery of a Weyl fermion semimetal and topological Fermi arcs. *Science* **349**, 613-617 (2015).
2. Lv, B. Q. et al. Observation of Weyl nodes in TaAs. *Nat. Phys.* **11**, 724-727 (2015).
3. Lv, B. Q. et al. Experimental Discovery of Weyl Semimetal TaAs. *Phys. Rev. X* **5**, 031013 (2015).
4. Yang, L. X. et al. Weyl semimetal phase in the non-centrosymmetric compound TaAs. *Nat. Phys.* **11**, 728-732 (2015).
5. Wan, X., Turner, A. M., Vishwanath, A. & Savrasov, S. Y. Topological semimetal and Fermi-arc surface states in the electronic structure of pyrochlore iridates. *Phys. Rev. B* **83**, 205101 (2011).
6. Xu, G., Weng, H., Wang, Z., Dai, X. & Fang, Z. Chern Semimetal and the Quantized Anomalous Hall Effect in HgCr₂Se₄. *Phys. Rev. Lett.* **107**, 186806 (2011).
7. Weng, H., Fang, C., Fang, Z., Bernevig, B. A. & Dai, X. Weyl Semimetal Phase in Noncentrosymmetric Transition-Metal Monophosphides. *Phys. Rev. X* **5**, 011029 (2015).
8. Nielsen, H. B. & Ninomiya, M. The Adler-Bell-Jackiw anomaly and Weyl fermions in a crystal. *Phys. Lett. B* **130**, 389-396 (1983).
9. Zyuzin, A. A. & Burkov, A. A. Topological response in Weyl semimetals and the chiral anomaly. *Phys. Rev. B* **86**, 115133 (2012).
10. Yang, K.-Y., Lu, Y.-M. & Ran, Y. Quantum Hall effects in a Weyl semimetal: Possible application in pyrochlore iridates. *Phys. Rev. B* **84**, 075129 (2011).
11. Huang, X. et al. Observation of the Chiral-Anomaly-Induced Negative Magnetoresistance in 3D Weyl Semimetal TaAs. *Phys. Rev. X* **5**, 031023 (2015).
12. Gao, Y., Yang, S. A. & Niu, Q. Intrinsic relative magnetoconductivity of nonmagnetic metals. *Phys. Rev. B* **95**, 165135 (2017).
13. Fang, C., Gilbert, M. J., Dai, X. & Bernevig, B. A. Multi-Weyl Topological Semimetals Stabilized by Point Group Symmetry. *Phys. Rev. Lett.* **108**, 266802 (2012).

14. Yu, Z.-M. et al. Encyclopedia of emergent particles in three-dimensional crystals. *Sci. Bull.* **67**, 375-380 (2022).
15. Zhang, T. et al. Double-Weyl Phonons in Transition-Metal Monosilicides. *Phys. Rev. Lett.* **120**, 016401 (2018).
16. Xiao, X. et al. Single pair of charge-2 high-fold fermions with surface type-II Van Hove singularities in ultralight chiral crystals. *Phys. Rev. B* **109**, 165136 (2024).
17. Sanchez, D. S. et al. Topological chiral crystals with helicoid-arc quantum states. *Nature* **567**, 500-505 (2019).
18. Jian, S.-K. & Yao, H. Fermion-induced quantum critical points in three-dimensional Weyl semimetals. *Phys. Rev. B* **96**, 155112 (2017).
19. de Juan, F., Grushin, A. G., Morimoto, T. & Moore, J. E. Quantized circular photogalvanic effect in Weyl semimetals. *Nat. Commun.* **8**, 15995 (2017).
20. Moon, E.-G., Xu, C., Kim, Y. B. & Balents, L. Non-Fermi-Liquid and Topological States with Strong Spin-Orbit Coupling. *Phys. Rev. Lett.* **111**, 206401 (2013).
21. Nielsen, H. B. & Ninomiya, M. Absence of neutrinos on a lattice: (I). Proof by homotopy theory. *Nucl. Phys. B* **185**, 20-40 (1981).
22. Nielsen, H. B. & Ninomiya, M. Absence of neutrinos on a lattice: (II). Intuitive topological proof. *Nucl. Phys. B* **193**, 173-194 (1981).
23. Liu, J. et al. Ideal type-I Weyl phonons in BaSO₄ with fewest Weyl points. *Phys. Rev. B* **109**, 045203 (2024).
24. Koepf, K. et al. TaIrTe₄: A ternary type-II Weyl semimetal. *Phys. Rev. B* **93**, 201101 (2016).
25. Belopolski, I. et al. Signatures of a time-reversal symmetric Weyl semimetal with only four Weyl points. *Nat. Commun.* **8**, 942 (2017).
26. Deaconu, D.-A., Shah, V., Belosludov, R. V. & Bahramy, M. S. Low-Symmetry Weyl Semimetals: A Path to Ideal Topological States. *Adv. Funct. Mater.* **n/a**, e06483.
27. Zhang, C. et al. Symmetry-guaranteed ideal Weyl semimetallic phase in face-centered orthogonal C₆. *Phys. Rev. B* **101**, 235119 (2020).
28. Fan, S., Fu, B., Ma, D.-S. & Wang, R. Complete topological phase diagram and realization of minimum Weyl nodes in a sheared chiral crystal of elemental tellurium. *Phys. Rev. B* **108**, 235211 (2023).
29. Wang, X. et al. Single pair of multi-Weyl points in nonmagnetic crystals. *Phys. Rev. B* **106**, 195129 (2022).
30. Yang, Y. et al. Ideal Unconventional Weyl Point in a Chiral Photonic Metamaterial. *Phys. Rev. Lett.* **125**, 143001 (2020).
31. Li, X.-P. et al. Observation of a single pair of type-III Weyl points in sonic crystals. *Phys. Rev. B* **106**, L220302 (2022).
32. Jin, Y. J. et al. Ferromagnetic Weyl semimetal phase in a tetragonal structure. *Phys. Rev. B* **96**, 201102(R) (2017).
33. Nie, S., Hashimoto, T. & Prinz, F. B. Magnetic Weyl Semimetal in K₂Mn₃(AsO₄)₃ with the Minimum Number of Weyl Points. *Phys. Rev. Lett.* **128**, 176401 (2022).
34. Ge, Y., Jin, Y. & Zhu, Z. Ferromagnetic Weyl metal in EuAgP. *Mater. Today Phys.* **22**, 100570 (2022).

35. Wang, L.-L. et al. Single pair of Weyl fermions in the half-metallic semimetal EuCd_2As_2 . *Phys. Rev. B* **99**, 245147 (2019).
36. Gao, Y. et al. Intrinsic ferromagnetic axion states and single pair of Weyl fermions in the stable-state $\text{MnX}_2\text{B}_2\text{T}_6$ family of materials. *Phys. Rev. B* **107**, 045136 (2023).
37. Armitage, N. P., Mele, E. J. & Vishwanath, A. Weyl and Dirac semimetals in three-dimensional solids. *Rev. Mod. Phys.* **90**, 015001 (2018).
38. Yan, B. & Felser, C. Topological Materials: Weyl Semimetals. *Annu. Rev. Condens. Matter Phys.* **8**, 337-354 (2017).
39. Oganov, A. R. et al. Ionic high-pressure form of elemental boron. *Nature* **457**, 863-867 (2009).
40. Häussermann, U., Simak, S. I., Ahuja, R. & Johansson, B. Metal-Nonmetal Transition in the Boron Group Elements. *Phys. Rev. Lett.* **90**, 065701 (2003).
41. Mouhat, F. & Coudert, F.-X. Necessary and sufficient elastic stability conditions in various crystal systems. *Phys. Rev. B* **90**, 224104 (2014).
42. Li, X.-P. et al. Type-III Weyl semimetals: $(\text{TaSe}_4)_2\text{I}$. *Phys. Rev. B* **103**, L081402 (2021).
43. Jin, Y. J., Xu, Y., Chen, Z. J. & Xu, H. Type-II quadratic and cubic Weyl fermions. *Phys. Rev. B* **105**, 035141 (2022).
44. Huang, S.-M. et al. New type of Weyl semimetal with quadratic double Weyl fermions. *Proc. Natl. Acad. Sci.* **113**, 1180-1185 (2016).
45. Blöchl, P. E. Projector augmented-wave method. *Phys. Rev. B* **50**, 17953-17979 (1994).
46. Kresse, G. & Furthmüller, J. Efficiency of ab-initio total energy calculations for metals and semiconductors using a plane-wave basis set. *Comput. Mater. Sci.* **6**, 15-50 (1996).
47. Perdew, J. P., Burke, K. & Ernzerhof, M. Generalized Gradient Approximation Made Simple. *Phys. Rev. Lett.* **77**, 3865 (1996).
48. Monkhorst, H. J. & Pack, J. D. Special points for Brillouin-zone integrations. *Phys. Rev. B* **13**, 5188-5192 (1976).
49. Togo, A., Oba, F. & Tanaka, I. First-principles calculations of the ferroelastic transition between rutile-type and CaCl_2 -type SiO_2 at high pressures. *Phys. Rev. B* **78**, 134106 (2008).
50. Evans, D. J. & Holian, B. L. The Nose–Hoover thermostat. *J. Chem. Phys.* **83**, 4069-4074 (1985).
51. Le Page, Y. & Saxe, P. Symmetry-general least-squares extraction of elastic data for strained materials from ab initio calculations of stress. *Phys. Rev. B* **65**, 104104 (2002).
52. Wu, Q., Zhang, S., Song, H.-F., Troyer, M. & Soluyanov, A. A. WannierTools: An open-source software package for novel topological materials. *Comput. Phys. Commun.* **224**, 405-416 (2018).
53. Mostofi, A. A. et al. wannier90: A tool for obtaining maximally-localised Wannier functions. *Comput. Phys. Commun.* **178**, 685-699 (2008).

Acknowledgements:

We wish to thank Weikang Wu and Shengyuan A. Yang for helpful discussions. This work was supported by the National Natural Science Foundation of China (Grants No. 12304202), Hebei Natural Science Foundation (Grant No. A2023203007), Science Research Project of Hebei Education Department (Grant No. BJK2024085), and Cultivation Project for Basic Research and Innovation of Yanshan University (No. 2022LGZD001).

Author contributions:

Hui-Jing Zheng proposed the HDSBC-B₂₀ and CR-B₁₂ structures and performed the corresponding DFT calculations. Yan Gao conceived the original ideas. Yanfeng Ge, Yong Liu, and Zhong-Yi Lu analyzed the results. Yan Gao writing-reviewing, conceptualization, supervision, and project administration. All authors discussed the results and commented on the manuscript at all stages.

Competing interests

The authors declare no competing financial interests.

Figures and Tables

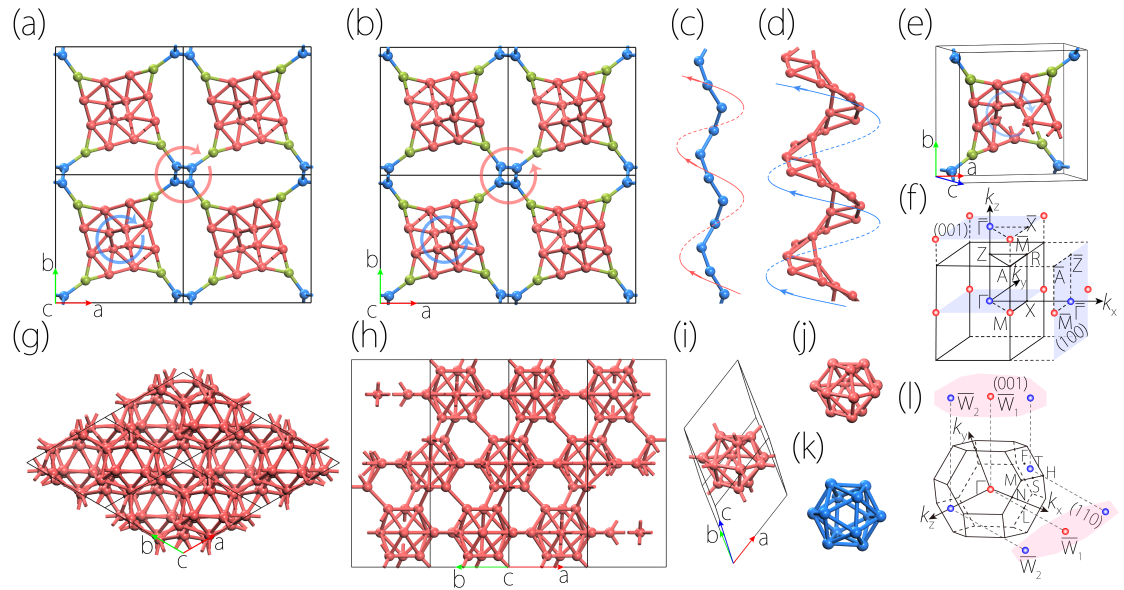


Figure 1 | Crystal structures and Brillouin zone (BZ) of HDSBC-B₂₀ with two enantiomeric left/right-handed structures and CR-B₁₂. (a) Top view of left-handed *l*-HDSBC-B₂₀. (b) Top view of right-handed *r*-HDSBC-B₂₀. (c) Single-atom-wide helical boron chain (blue) of *l*-HDSBC-B₂₀. (d) Double-atom-wide helical boron chain (red) of *l*-HDSBC-B₂₀. (e) Perspective view of the unit cell of *l*-HDSBC-B₂₀. (f) Distribution of Weyl points of *l*-HDSBC-B₂₀ in the 3D BZ showing $C = -2$ and $C = +2$ at Γ and M positions, respectively, and their projections on the (001) and (100) surfaces. (g) Top and (h) side views of the $2 \times 2 \times 1$ conventional cell of CR-B₁₂. (i) Primitive cell of CR-B₁₂. (j) Basic structural unit of CR-B₁₂ (red). (k) Basic structural unit of α -B₁₂ (blue). (l) Distribution of Weyl points in the bulk BZ of CR-B₁₂ and their projections on the (001) and (110) surfaces.

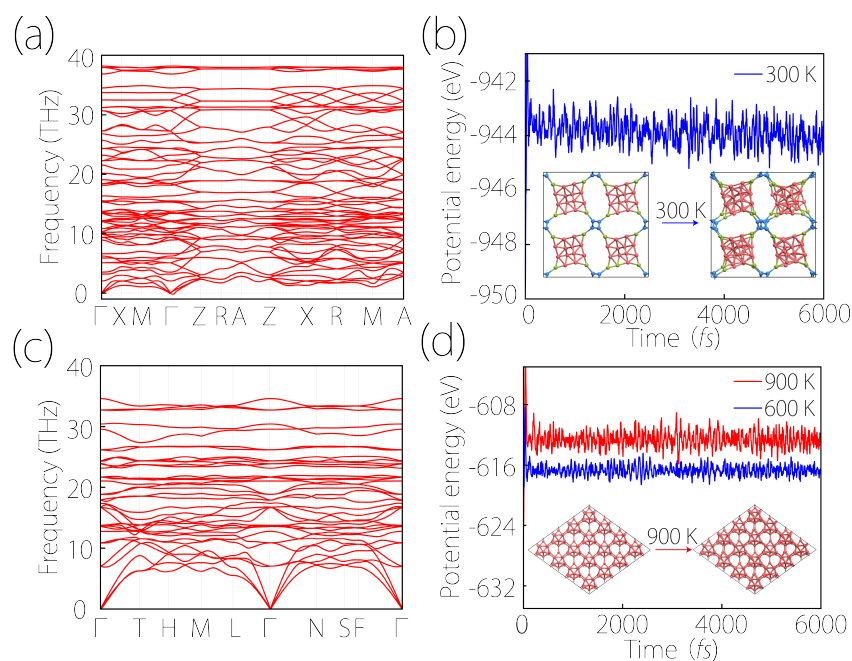


Figure 2 | Dynamic and thermal stability of HDSBC-B₂₀ and CR-B₁₂. (a) Phonon dispersion of HDSBC-B₂₀ along the entire high-symmetry path. (b) Total potential energy fluctuation in *ab initio* molecular dynamics (AIMD) simulations of HDSBC-B₂₀ at 300 K. The inset shows the equilibrium atomic configuration after 6000 fs relaxation at 300 K. (c) Phonon dispersion of CR-B₁₂ along the entire high-symmetry path. (d) Total potential energy fluctuations in AIMD simulations of CR-B₁₂ at 900 K and 600 K, respectively. The inset shows the equilibrium atomic configuration after 6000 fs relaxation at 900 K.

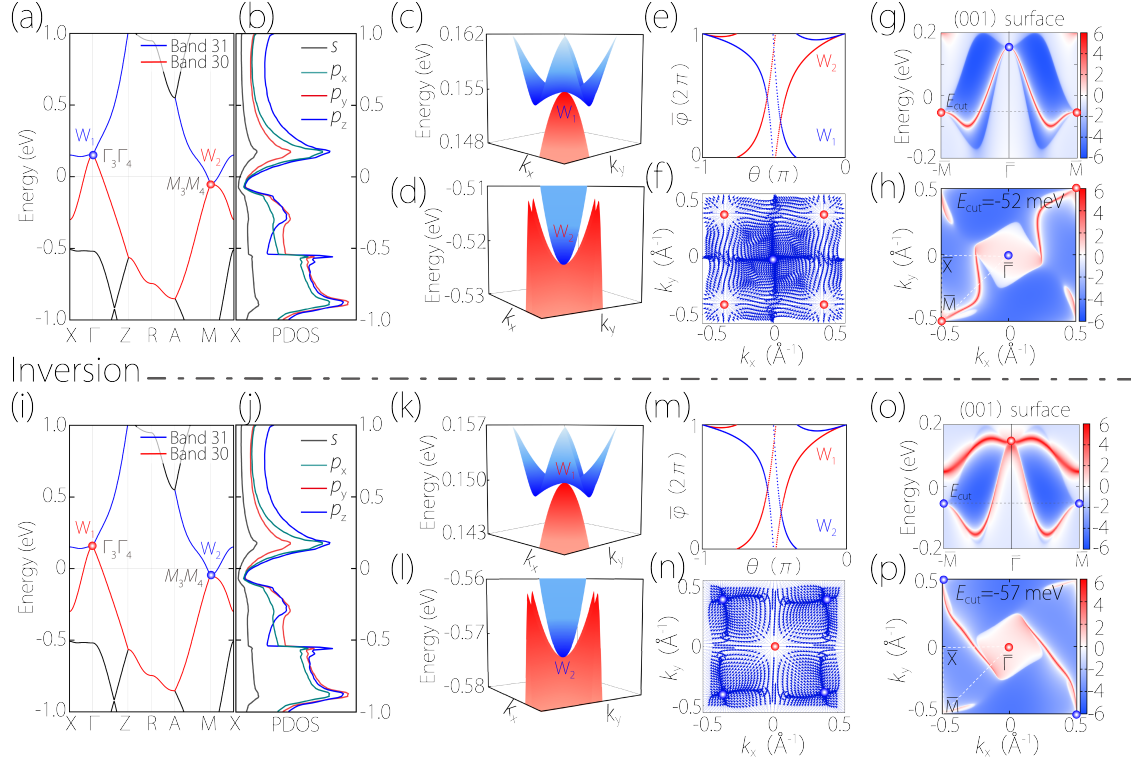


Figure 3 | Electronic and topological properties of the chiral boron allotropes *l*-HDSBC- B_{20} and *r*-HDSBC- B_{20} . (a-h) Calculated electronic and topological properties for the left-handed *l*-HDSBC- B_{20} . (a) Band structure of *l*-HDSBC- B_{20} along high-symmetry paths. Weyl points W_1 (blue dot) and W_2 (red dot) are formed by the crossing of the highest occupied 30th band and lowest unoccupied 31st band at time-reversal invariant points Γ and M . (b) Projected density of states (PDOS) of *l*-HDSBC- B_{20} . (c-d) 3D band structures showing quadratic dispersion characteristics of W_1 and W_2 bands in the k_x - k_y plane, respectively. (e) Evolution of Wannier charge centers (WCCs) on spheres enclosing W_1 and W_2 , showing topological charges of -2 and +2, respectively. (f) Berry curvature distribution in the $k_z = 0$ plane of *l*-HDSBC- B_{20} . (g) Calculated surface band structure of the (001) surface. The dashed line indicates the band energy corresponding to Fig. 3(h). (h) Fermi arcs at the energy slice $E = -52$ meV (i.e., the energy of W_2) on the (001) surface. (i-p) The right-handed *r*-HDSBC- B_{20} structure related by space inversion exhibits similar electronic and topological properties to the left-handed *l*-HDSBC- B_{20} , except for the reversed chirality of Weyl points.

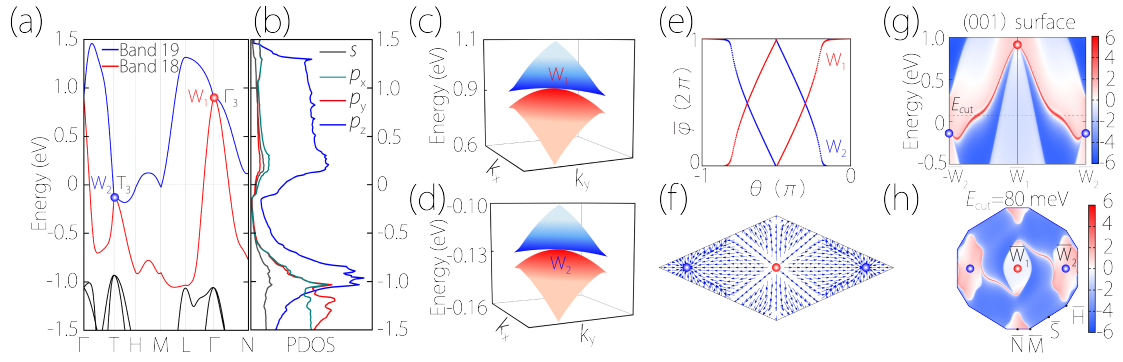


Figure 4 | Electronic and topological properties of CR-B₁₂. (a) Band structure of CR-B₁₂ along high-symmetry paths. Weyl points W₁ (red dot) and W₂ (blue dot) are formed by the crossing of the highest occupied 18th band and lowest unoccupied 19th band at time-reversal invariant points Γ and T. (b) Projected density of states (PDOS) of CR-B₁₂. (c-d) 3D band structures showing quadratic dispersion characteristics of W₁ and W₂ bands in the k_x - k_y plane, respectively. (e) Evolution of Wannier charge centers on spheres enclosing W₁ and W₂, generating topological charges of +2 and -2, respectively. (f) Berry curvature distribution in the plane containing W₁ and W₂, confirming W₁ as a source and W₂ as a sink. (g) Calculated surface band structure of the (001) surface. The dashed line indicates the energy level corresponding to Fig. 4(h). (h) Fermi arcs at the energy slice $E = 80$ meV on the (001) surface.